International Journal of Current Science Research and Review
ISSN: 2581-8341
Volume 08 Issue 10 October 2025
DOI: 10.47191/ijcsrr/V8-i10-18, Impact Factor: 8.048
IJCSRR @ 2025
www.ijcsrr.org

Geospatial Assessment of Three Decades of Shoreline Shifts and Two Decades of Vegetation Change in the Grand Saloum Transboundary Wetland Complex, Senegal-The Gambia

Ousmane Badji[1*], Adam Ceesay[2], Kwame Oppong Hackman[3]
[1]WASCAL Graduate Research Programme on Climate Change and Land Use, Department of Civil Engineering, Kwame Nkrumah University of Science and Technology, Kumasi, Ghana
[2]Institut des Sciences de l'Environnement, Cheikh Anta Diop University (UCAD)
[3]Competence Center, West African Science Service Center on Climate Change and Adapted Land Use (WASCAL), Ouagadougou, Burkina Faso

ABSTRACT: Coastal wetlands at the land–sea interface are on the frontline of climate change, yet integrated evidence on geomorphic and ecological responses remains limited in West Africa. We quantified shoreline trajectories (1990–2020) and land-cover dynamics (2000–2020) across the transboundary Grand Saloum complex (Senegal–The Gambia) using Landsat surface-reflectance time series, spectral indices (NDVI, NDWI, NDBI), and the Digital Shoreline Analysis System (DSAS). Shorelines were extracted from NDWI-based water masks, filtered and vectorized, then analyzed in DSAS with End Point Rate statistics. Vegetation was mapped in Google Earth Engine with a Random Forest classifier (mangrove, other vegetation, built/bare, water). The coastline is dominated by erosion (mean −2.44 m·yr^{-1}) interspersed with localized accretion (mean +1.84 m·yr^{-1}). Erosion hotspots concentrate in central sectors, whereas mixed erosion–accretion patterns occur near the northern and southern mouths. Concurrently, mangrove cover expanded from 57,867.61 ha in 2000 to 66,840.17 ha in 2020 (~+15.5%), while other vegetation declined from 23,483.18 ha to 16,146.11 ha (~−31.3%). Within a 1-km coastal buffer, mangroves remained broadly stable to slightly increasing (16.43%→16.81%). These findings depict a dynamic yet resilient system where mangrove gains coexist with heterogeneous shoreline retreat and conversion of non-mangrove covers to bare substrates and water. Management should safeguard landward migration corridors, target erosion-prone reaches with nature-based measures, and institutionalize a transboundary monitoring, reporting, and verification framework that updates DSAS and satellite products at 2–3-year intervals while integrating in-situ elevation, salinity, and sediment data. Our workflow provides transferable, decision-relevant evidence for coastal adaptation and blue-carbon planning in data-limited deltas and policy design.

KEYWORDS: Coastal erosion, Shoreline change, Mangroves, Remote sensing, DSAS, Landsat, Google Earth Engine, Grand Saloum (Senegal–The Gambia).

1. INTRODUCTION

Coastal wetlands at the land–sea interface are on the frontline of climate change. Rising seas, driven by ocean thermal expansion and accelerating land-ice loss, are altering shoreline position, inundation regimes, and salinity gradients that structure wetland ecosystems (Church et al., 2001). These physical shifts cascade into ecological and livelihood impacts for communities dependent on fisheries, agriculture, and coastal protection; conversely, slower relative sea-level rise can expand the window for adaptation in deltas and low-lying coasts ((IPCC, 2007, 2023).

Mangrove ecosystems are both climate sentinels and buffers: they sequester carbon, attenuate waves, and sustain coastal economies, yet they are sensitive to changes in hydrodynamics and salinity (Ellison, 2014). Prolonged or more frequent inundation and salinity shifts can exceed species-specific tolerance thresholds, triggering dieback or community reassembly unless sediment accretion and landward migration keep pace (Friess et al., 2012). These responses vary regionally, underscoring the need for site-specific, decadal monitoring (Ellison, 2014; Friess et al., 2012).

In West Africa, and Senegal in particular, coastal risks have intensified, threatening settlements and critical habitats. Along sectors of the Senegalese coast, multi-year analyses report shoreline retreats commonly on the order of 1–2 m·yr^{-1} (Diop et al.,

International Journal of Current Science Research and Review
ISSN: 2581-8341
Volume 08 Issue 10 October 2025
DOI: 10.47191/ijcsrr/V8-i10-18, Impact Factor: 8.048
IJCSRR @ 2025
www.ijcsrr.org

2014; P. W. Bakhoum et al., 2017). A notable morphological shift in the Saloum system was the 1987 storm-breach of the Sangomar spit, which reconfigured connectivity and sediment dynamics (MEPN, 2006). Scenario analyses further suggest substantial potential loss of low-lying areas under sea-level rise in the Saloum estuary and significant erosion pressure along the Senegal–Gambia border (Jallow et al., 1996; Niang et al., 2010).

The Grand Saloum, encompassing Senegal's Saloum Delta Biosphere Reserve and The Gambia's Niumi National Park, forms a transboundary Ramsar wetland complex of high ecological and economic value. Although numerous studies have addressed threats, pressures, and climate–mangrove linkages in parts of the system (Drame & Sambou, 2013; SIDIBE, 2010; Sow & Ba, 2019), an integrated, geospatially explicit assessment that couples three decades of shoreline dynamics with two decades of vegetation change remains limited. This study addresses that gap by leveraging satellite remote sensing and GIS to quantify shoreline trajectories (1990–2020) and vegetation dynamics with emphasis on mangroves (2000–2020), providing a decision-relevant geospatial evidence base for coastal management in the Grand Saloum (Ceesay et al., 2017).

2. METHODOLOGY

2.1. Study area

The Grand Saloum transboundary complex (Figure 1) covers an area of 83,758 ha. It is composed of:

- The Saloum Delta National Park (PNDS) in Senegal, which is located between latitudes 13.583333 and 13.916667, and longitudes 16.466667 and 16.083333. This site was erected by a Decree under the Senegalese law N°76 577 on 28th March 1976 and covered a total of 76,000 ha.
- The Niumi National Park (NNP) in The Gambia, which is located between latitudes 13.516667 and 13.983333 and longitudes 16.933333 and 16.083333, is a coastal strip of 7758 ha erected as a National Park in 1986 and a RAMSAR Site in October 2008. It is the natural southern extension of the Saloum National Park (PNDS) (WOW, 2015).

2.2. Climate

The Grand Saloum transboundary complex is marked by a Sudano-Sahelian climate type characterised by rainfall values between 400 and 800 mm with an average temperature of 29° C. The rainfall is generally less in the northern part of the complex (Saloum) and greater in the southern region (Niumi). The Canary current coastal influence is much more prominent on the Senegalese section of the complex. Two main seasons characterise the climate:

- A dry season (cold from November to March, hot from March to June), where the prevailing winds are maritime trade winds, fresh (in a north to north-west direction)
- A dry continental winds (in an east to north-east direction, known as Harmattan).
- A hot, humid rainy season from July to October, dominated by monsoon winds (direction: West and southwest). Annual rainfall in the Saloum Delta has declined from a range of 600-900 mm for the period 1931- 1960 to less than 400-600 mm today. There is a total of 50-60 days of rain per year, with maximum rainfall in August. Recently, in Niumi, there have been reports of increased annual average rainfall from 2000 to 2010, and this certainly might be the same at the whole complex level. Average annual temperatures vary between 26 and 31° C (WOW, 2015).

International Journal of Current Science Research and Review
ISSN: 2581-8341
Volume 08 Issue 10 October 2025
DOI: 10.47191/ijcsrr/V8-i10-18, Impact Factor: 8.048
IJCSRR @ 2025
www.ijcsrr.org

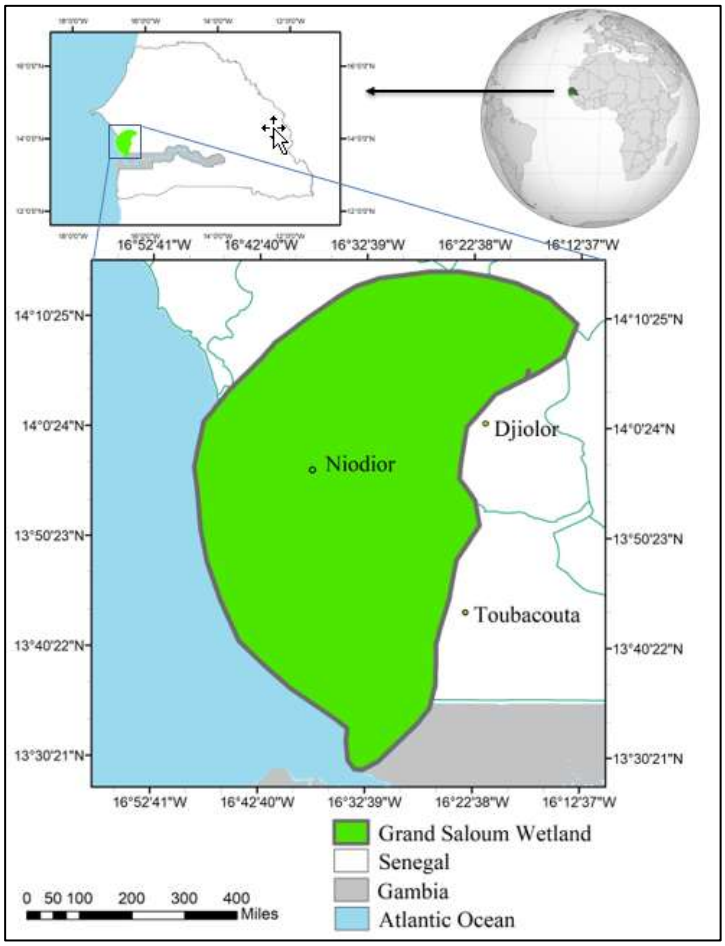

Figure 1: Map of the study area (Saloum-Nuimi Transboundary Ramsar Complex)

2.3. Remote sensing of the shoreline dynamic

2.3.1. Satellite images

Satellite images with different spatial resolutions processed with various change analysis methods are effective for quantifying changes in the wetland (Toure et al., 2018). Accordingly, surface reflectance images from Landsat 5, 7, and 8 (Table 1) between 1990 and 2020 were accessed and processed in ENVI.

Table 1: Landsat images properties

Dates and time of acquisition	Paths and Rows	Cloud Cover	Sensors	Data Provider:	Bands
1990-12-21 10:47:02	(PATH: 205, ROW: 50) & (PATH: 205, ROW: 51)	0	Landsat 5	USGS	Blue, Green, Red, NIR, SWIR-1, SWIR-2, NDVI, NDBI, NDWI
2000-12-08 11:17:48		0	Landsat 7		

International Journal of Current Science Research and Review
ISSN: 2581-8341
Volume 08 Issue 10 October 2025
DOI: 10.47191/ijcsrr/V8-i10-18, Impact Factor: 8.048
IJCSRR @ 2025
www.ijcsrr.org

2010-12-28 11:17:22	0	Landsat 5
2020-12-07 11:27:49	0	Landsat 8

2.3.2. Image pre-processing

The bands in the surface reflectance images were atmospherically corrected and orthorectified. At any pixel location, the value recorded on a remotely sensed image does not refer to the true ground-leaving radiance at that particular point. One part of the brightness is due to the target of interest reflectance and the remainder from the atmosphere itself. Their contributions are not known a priori, so the objective of atmospheric correction was to quantify these two components in order to use correct target reflectance (Themistocleous et al., 2008). The orthorectification is necessary because of deformations mainly due to camera distortions and acquisition geometry.

The terrain-related geometric distortions that were removed during the orthorecfication stage are related to the image formation process (error tracking), such as distortions caused by the platform, and mainly related to the variation of the elliptic movement around the Earth, instantaneous field of view, topographic relief changes, etc. (Chmiel et al., 2004).

2.3.3. Data analysis and processing

Spectral indices, also known as band transformations, were obtained from the Landsat 5, 7, and 8 surface reflectance images by the following equations (Table 2).

Table 2: Formulas for the NDVI, NDWI, and NDBI calculation

Index Used	Equations
NDVI	$NDVI = \frac{\rho_{NIR} - \rho_{RED}}{\rho_{NIR} + \rho_{RED}}$
NDWI	$NDWI = \frac{\rho_{Green} - \rho_{NIR}}{\rho_{Green} + \rho_{NIR}}$
NDBI	$NDBI = \frac{\rho_{SWIR1} - \rho_{NIR}}{\rho_{SWIR1} + \rho_{NIR}}$

With: ρ_Green=ToA reflectance of green band, **ρ_NIR**=ToA reflectance of near infrared band.
ρ_NIR=ToA reflectance of near infrared band **ρ_SWIR1**= short-wave infrared

2.4. Shoreline Detection and analysis

2.4.1. Shoreline processing

DSAS is one of the most efficient and effective as well as less time-consuming tools in shoreline change analysis compared with the many traditional tools and methods and produces results of better accuracy (Sekovski et al., 2014). It relies on input data such as the date and year and a digitized geometry (in shapefile format) of the shoreline. A series of processes were carried out to analyse the changes in the shoreline, as given in Figure 2.

➔Segregation of water and non-water feature using a spectral index

NDWI, as defined mathematically in Table 2, was used to determine the water and non-water features. NDWI value ranges from −1 to +1. The NDWI image typically provides positive results for water features and negative for non-water features (McFEETERS, 1996). Only water and non-water features are required to delineate the separation line as a shoreline, and therefore a binary image classification, i.e., 0 and 1, was performed for depicting non-water and water features (Ji et al., 2009).

International Journal of Current Science Research and Review
ISSN: 2581-8341
Volume 08 Issue 10 October 2025
DOI: 10.47191/ijcsrr/V8-i10-18, Impact Factor: 8.048
IJCSRR @ 2025
www.ijcsrr.org

➔Post-processing of binary raster image

A 3 × 3 mode filter was applied for the post-processing operation that substituted the isolated pixels to the most common neighboring class (either water class or non-water class) to decompose the scattered and isolated pixels (Bartuś, 2014). The jagged boundaries of the water and non-water classes were smoothened by using QGIS clean tool. The shoreline vector was then produced using a raster binary image, and the abutting line of water and non-water class was traced to extract the final shoreline.

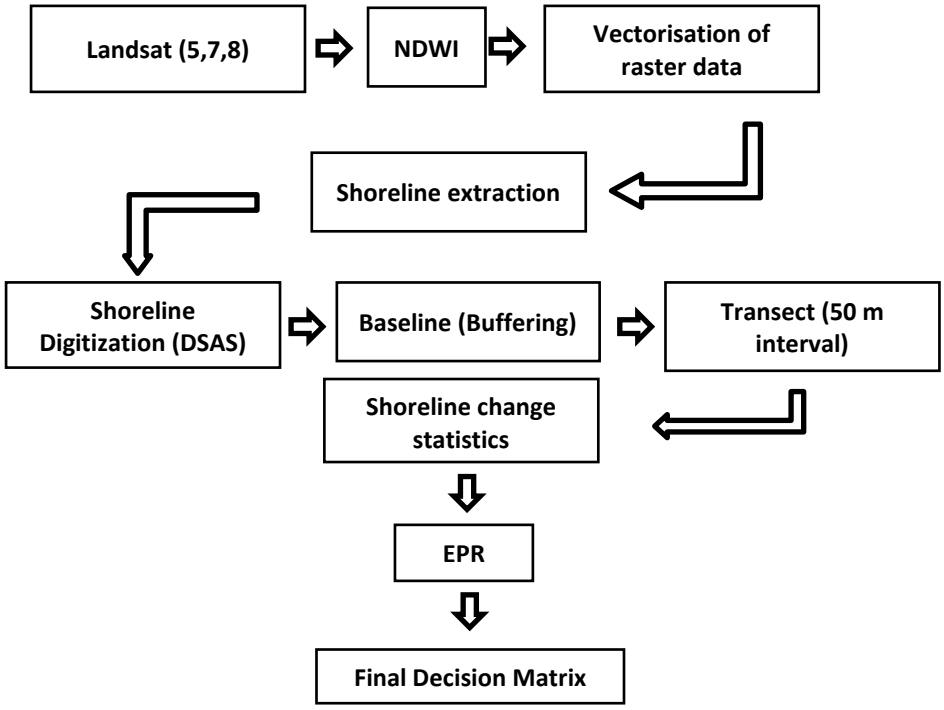

Figure 2: Shoreline detection and analysis process

➔Shoreline generation

After that, the different time periods shoreline data was fed to the DSAS for further computation of shoreline change for 30 years from 1990 to 2020. In the DSAS tool, shorelines positions are compiled with five attribute fields which include Object ID (a unique number assigned to each), shape (polygon), date (original survey year), and shape length, and uncertainty values. Shorelines of different years were merged as a single feature, which creates a single shapefile of the multiple shorelines. The baseline was generated for calculating the shoreline change by closely digitizing the direction and shape of the outer shoreline. From this process, the rates of shoreline change were generated.

➔Shoreline change statistics

The calculation of the shoreline change was done in the form of End point Rate (EPR). The final decision matrix was prepared on the basis of the results and output. EPR formula (equation 1) was used to present the computational results. The DSAS tool itself chooses the shoreline transects, gives them dependent and independent variables, and automatically calculates (EPR) the rates of erosion and deposition. The accuracy level would be as high as when more years satellite data set has been incorporated (Sekovski et al. 2014). For example, 4 years of satellite images were chosen for the shoreline change analysis. A ± 5 m uncertainty and 95% confidence interval was set as default parameter to calculate the statistics.

$$\mathbf{EPR} = \frac{\text{Distance in metres (m)}}{\text{time between oldest and most recent shoreline(Year)}} \quad \textbf{Eq. (1)}$$

The EPR values can either be positive or negative, where a positive value represents seaward or offshore movement, and a negative value represents landward movement.

International Journal of Current Science Research and Review
ISSN: 2581-8341
Volume 08 Issue 10 October 2025
DOI: 10.47191/ijcsrr/V8-i10-18, Impact Factor: 8.048
IJCSRR @ 2025
www.ijcsrr.org

3.4. Remote sensing of the vegetation dynamic

3.4.1. Image classification features

Due to the long record of continuous observation and high spatial resolution, the Landsat series of satellite images are one of the most useful data for biodiversity assessment (Hackman et al., 2017) and widely used in wetland change assessments (Ajaj et al., 2017; Ceesay et al., 2017). The Tier 1 surface reflectance images from the Landsat series of satellites available in GEE were used because surface reflectance gives the most accurate information about the surface characteristics. In addition, three spectral indices (NDWI, NDVI, and NDBI) obtained from the Landsat 5, 7, and 8 surface reflectance images (see Table 2) were used as features. Because the study area is a wetland, the 30m spatial resolution digital elevation model (DEM) from the NASA Shuttle Radar Topography Mission (SRTM) was added to the feature space to distinguish mangrove from other vegetation. Thus, in all the feature space was a 10-band image stack made up of six surface reflectance bands (Blue, Green, Red, Near infrared, SWIR-1, and SWIR-2), three spectral indices, and the DEM.

3.4.2. Image pre-processing

Prior to their ingestion in GEE, the surface reflectance images from the three Landsat sensors were atmospherically corrected using the Landsat Ecosystem Disturbance Adaptive Processing System (LEDAPS) or the Land Surface Reflectance Code (LaSRC). Also, the visible bands were bands processed to orthorectified surface reflectance. The bands from Landsat 8 were renamed to match those in Landsat 5 and 7. It was impossible to get cloud-free Landsat images for the study area. As a result, the clouds in all available images were masked. Finally, for each year, the complete collection of images from the Landsat sensors was merged using the median filter. In this way, clean Landsat composites were obtained for each year from 2000 to 2020 for use as inputs to the image classification work.

3.4.3. Training and testing sample collection

Training and testing samples were manually collected using the high-resolution orthophotos on Google Earth (GE). The sample collection protocol was used as the following:

- Generate simple random points within the study area.
- Visually inspect the land use at all points with at least 30m radius homogeneous neighborhood, and accept/reject based on local knowledge.
- Split samples into training and testing sets.

3.4.4. Image classification

A supervised classifier (Random Forest) was used for the land-cover classification on a pixel-by-pixel basis. Apart from its availability in Google Earth Engine, this classifier was selected because they are widely used in land-cover classification (Jia et al., 2014; Yu et al., 2013). The classification workflow is provided in Figure 3 below.

In order to make the map of the land-cover classification of the Grand Saloum the classified maps have been exported from GEE to ArcGIS 10.4. Four (4) classes have been taken into accounts such as mangrove, other vegetation, built and bare sand, and water.

To access the vegetation close to the shoreline, a buffer has been manually created for a distance of 1km from the shoreline. Zooming of the classified map along the shoreline has been done to detect areas of great change.

3.4.5. Accuracy assessment

The accuracy was tested using an independent set of samples that were randomly selected from the training and testing samples and computed the confusion matrix for each classified map. The classification procedure was done in Google Earth Engine while testing procedure were carried out in ArcGIS 10.4. For accuracy, 65% of sampling points were used for training and 35% for testing. The accuracy was calculated using the following formula:

$$\textbf{Accuracy}\ (\%) = \frac{\textbf{Total True Value Pixels}}{\textbf{Total Sample Value Samples}}\ \textbf{x 100} \quad \textbf{Eq(2)}$$

International Journal of Current Science Research and Review
ISSN: 2581-8341
Volume 08 Issue 10 October 2025
DOI: 10.47191/ijcsrr/V8-i10-18, Impact Factor: 8.048
IJCSRR @ 2025
www.ijcsrr.org

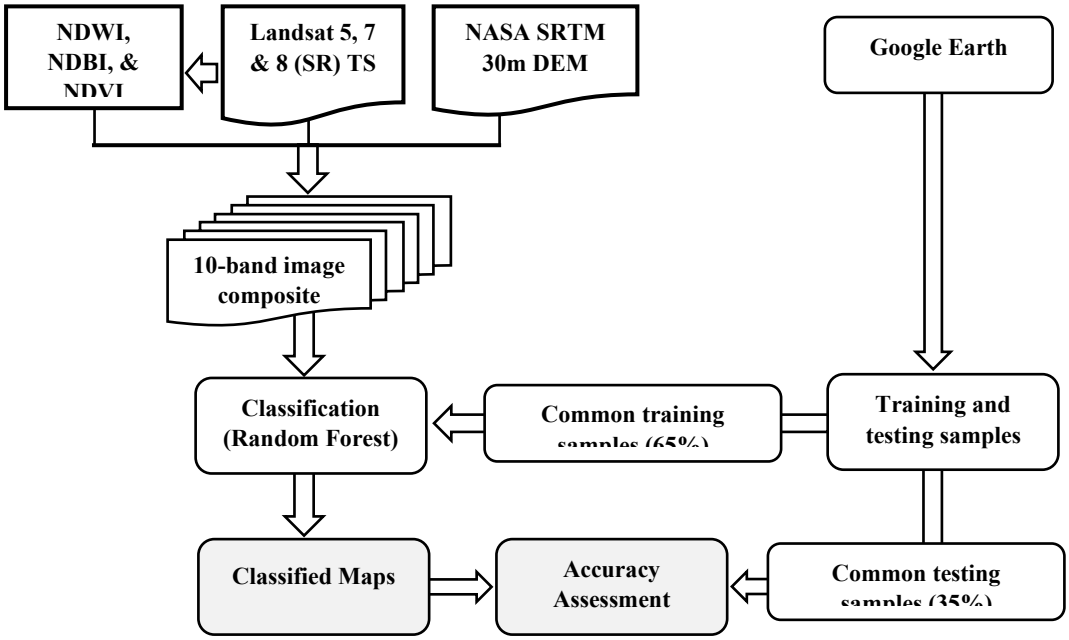

Figure 3: Landsat image classification process

4. RESULTS

4.1. Shoreline dynamic

4.1.1. General observation in the shoreline changes

The studied segment includes the Djiffer coast (Sector E) and goes as far as Dionewar (Sector D), Niodior (Sector C), Bettenty (Sector B), and Djinack Bara and Jinack Kajata Island northern coast of the Gambia (Sector A). Between 1990 and 2020, erosion and accretion occurred in some places and the ecosystem is highly dominated by erosion. Figure 4 highlights five main sections highly dynamic. Sector A and E show Moderate to High erosion and accretion. The sector B, C, and D are characterised by moderate to high erosion at some points. For this purpose, an annual average erosion rate of 2.44 m is observed and an average accretion rate of 1.84 m.

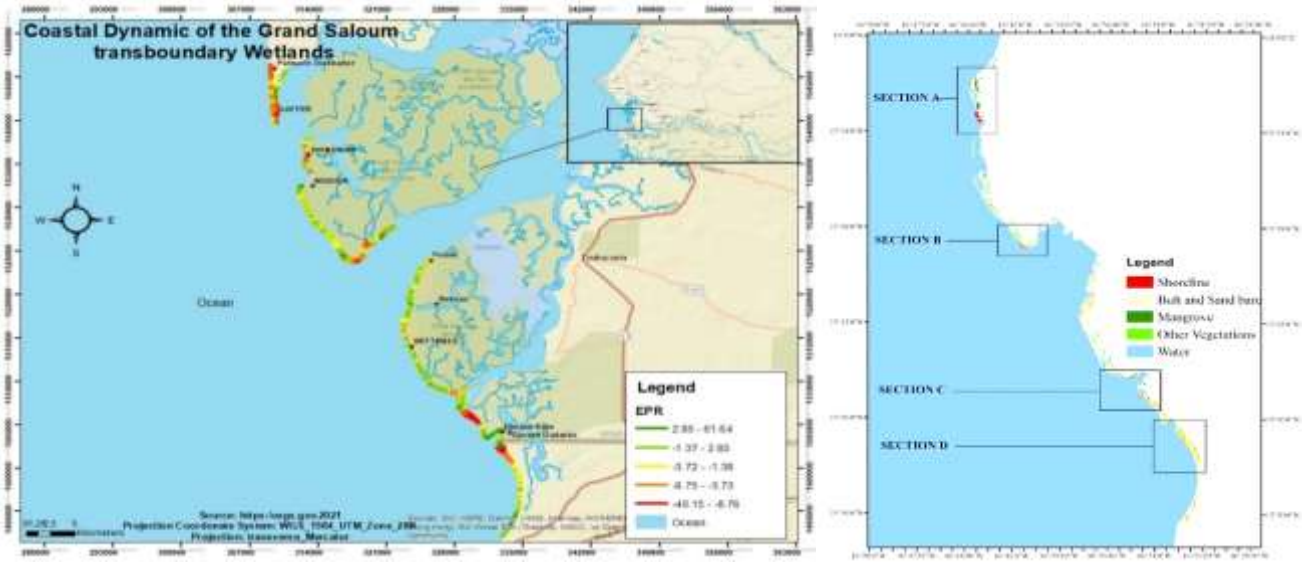

Figure 1: Point of erosion (Red) and accretion (Dark Green) along the Grand Saloum Shoreline

International Journal of Current Science Research and Review
ISSN: 2581-8341
Volume 08 Issue 10 October 2025
DOI: 10.47191/ijcsrr/V8-i10-18, Impact Factor: 8.048
IJCSRR @ 2025
www.ijcsrr.org

4.1.2. Sectorial Analysis

Table 3 shows information related to the rate of change in the shoreline occurring in each section. Sections A and E showed a balance erosion of 4.13 ±0.47 and 1.62 ±0.47 respectively and accretion of 2.82 ±0.47 for both sections. Sections C and D are characterised by High rate of erosion with an average of 2.39 ±0.47 and 2.63 ±0.47, respectively. The average accretion for sections C and D range between 1.45 ±0.47 and 1.018 ±0.47, respectively. Section B doesn't show so much dynamic with an average erosion and accretion of 1.41 ±0.47 and 1.12 ±0.47.

Table 3: Parameters of shoreline dynamics calculated in each transect

Region	A	B	C	D	E
Transect	1-481	482-914	915- 1276	1277 -1391	1392 - 1490
Number of transect	481	433	362	114	98
Average Accretion (m/yr)	2.82 ±0.47	1.12 ±0.47	1.45 ±0.47	1.02 ±0.47	2.82 ±0.47
Average Erosion (m/yr)	-4.13 ±0.47	-1.41 ±0.47	-2.39 ±0.47	-2.63 ±0.47	-1.62 ±0.47
Max. accretion (m/yr) (transect)	14.52 ±0.47	2.7 ±0.47	2.8 ±0.47	2 ±0.47	4.98 ±0.47
Max. erosion (m/yr) (transect)	-47.28 ±0.47	-4.53 ±0.47	-12.02 ±0.47	-9.09 ±0.47	-4.02 ±0.47

4.2. Vegetation dynamic

4.2.1. Analysis of the changes in the whole transboundary wetlands

Figures 5 and 6 show that from 2000 to 2020 the whole Grand Saloum wetlands experienced an increase in mangrove vegetation and a decrease in the other vegetation. The figures show estimated mangrove coverages of 57867.61 ha and 66840.17 ha in 2000 and 2020 respectively. The coverage of the other vegetation has reduced from 2000 to 2020 with an estimated coverage of 23483.18 ha to 16146.11 ha respectively. The accuracies of the classification vary between 97.51 % and 99.37 % .

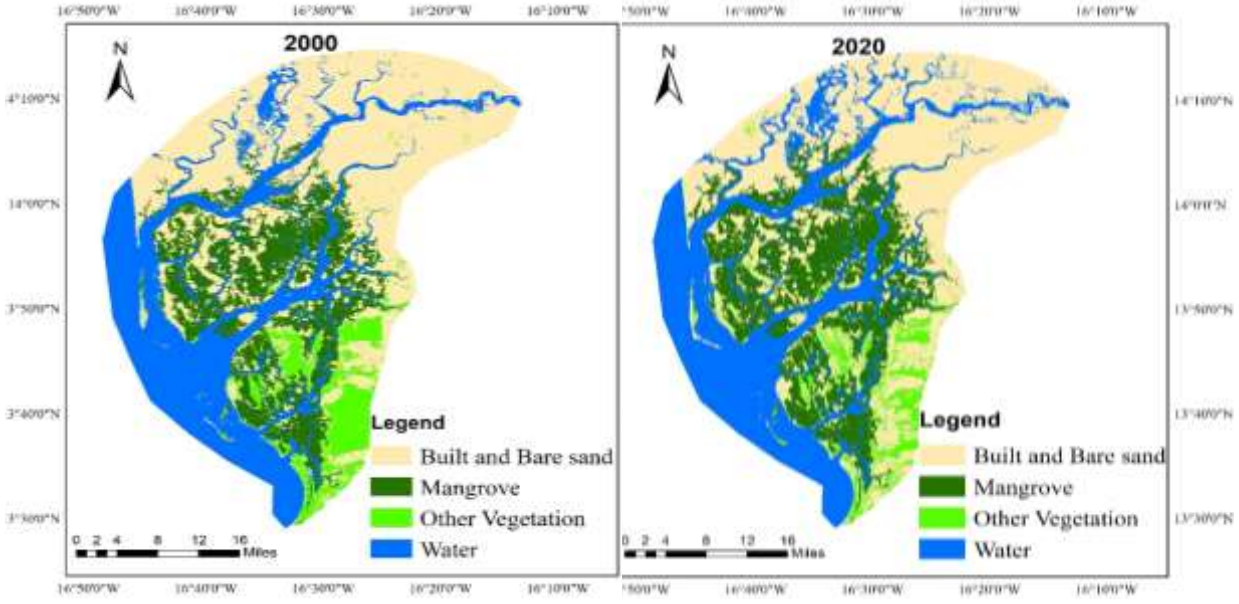

Figure 5: Map of the mangrove and other vegetation for 2000 and 2020

International Journal of Current Science Research and Review
ISSN: 2581-8341
Volume 08 Issue 10 October 2025
DOI: 10.47191/ijcsrr/V8-i10-18, Impact Factor: 8.048
IJCSRR @ 2025
www.ijcsrr.org

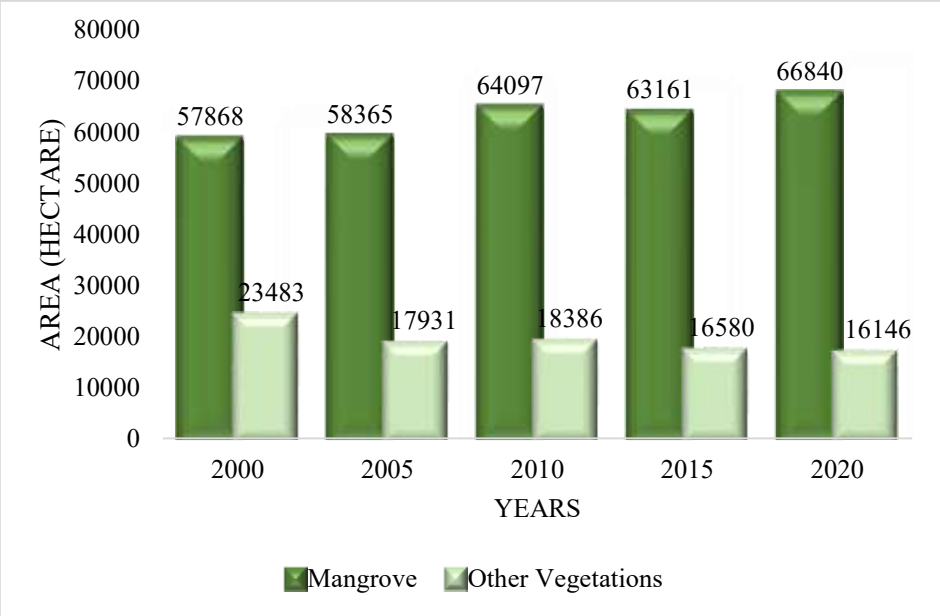

Figure 6: vegetation dynamics of the Grand Saloum

The resulting map (Figure 7) from the change detection analysis shows an increase of mangrove northward and a decrease of the other vegetation southward.

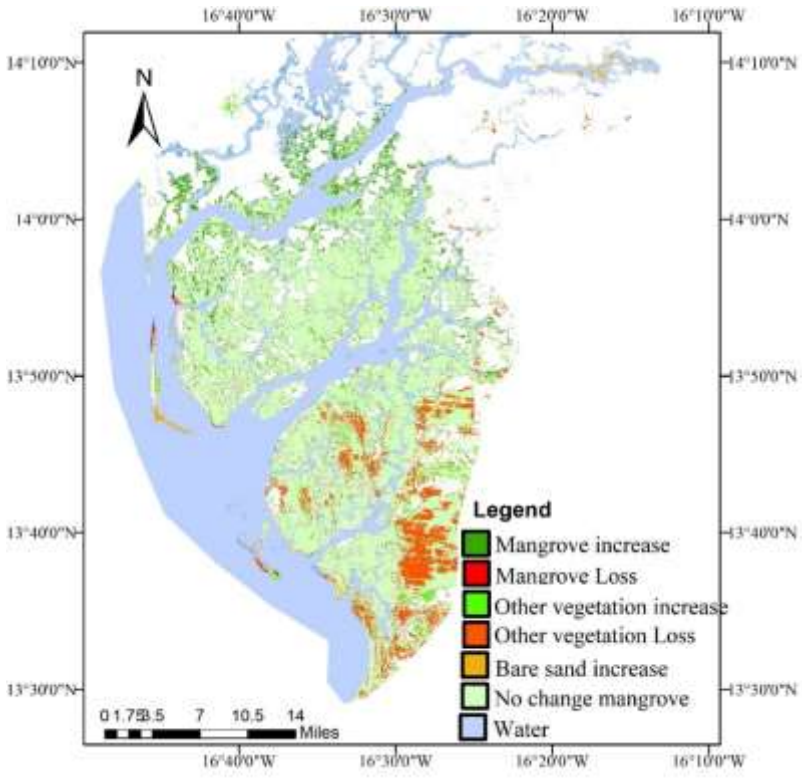

Figure 7: Change detection analysis of the vegetation from 2000 to 2020

International Journal of Current Science Research and Review
ISSN: 2581-8341
Volume 08 Issue 10 October 2025
DOI: 10.47191/ijcsrr/V8-i10-18, Impact Factor: 8.048
IJCSRR @ 2025
www.ijcsrr.org

4.2.2. Analysis of the changes in vegetation close to the shoreline

Figure 8 shows the estimated coastal vegetation close to the shoreline. The result shows a decrease in the mangrove area from 16.43% in 2000 to 15.17% in 2005. The mangrove area increased slightly from 16.37% in 2010 to 16.81% in 2020. Regarding the other vegetation cover, a decrease was noticed from 9.52% in 2000 to 6.52% in 2005. From 2005 the other vegetation cover evolved with slightly increasing and decreasing phases.

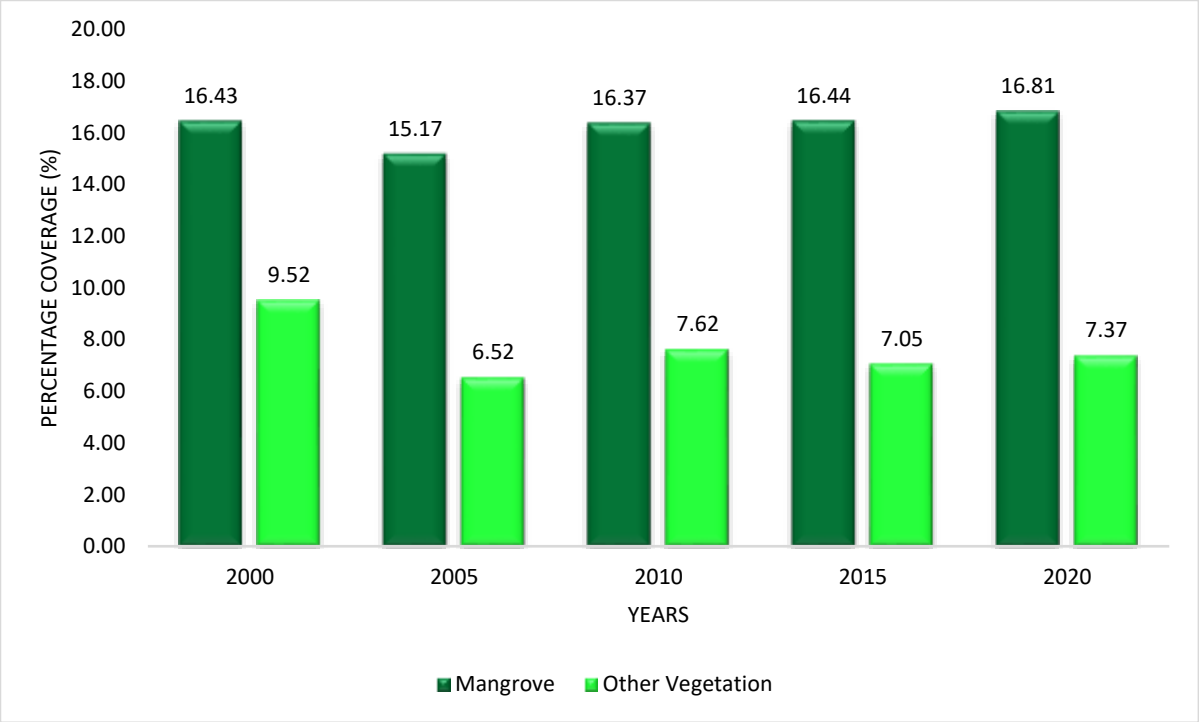

Figure 8: Dynamic of mangrove and other vegetation close to the shoreline from 2000 to 2020

4.2.2.1. Change detection

The conversion matrix (Table 4) shows that 3.07% of the mangrove coverage has changed to bare sand area and 3.44% eroded by the water. For the other vegetation, the conversion has been dominated by bare sand with 37.49%.

The change detection map shows some major changes on both mangrove and other vegetation (Figure 9). In the map, the loss of mangrove is mainly pronounced in sections A and B. Section D is mostly dominated by the loss of the other vegetation.

Table 4: Transition matrix between 2000 and 2020 (In percent)

	Initial year			
LULC (%)	Mangrove	Other vegetation	Built and bare sand	Water
Mangrove	92.62	2.42	6.06	0.46
Other vegetation	0.86	58.62	8.86	0.03
Built and bare sand	**3.07**	**37.49**	73.44	1.89
Water	**3.44**	1.46	11.64	97.61

International Journal of Current Science Research and Review
ISSN: 2581-8341
Volume 08 Issue 10 October 2025
DOI: 10.47191/ijcsrr/V8-i10-18, Impact Factor: 8.048
IJCSRR @ 2025
www.ijcsrr.org

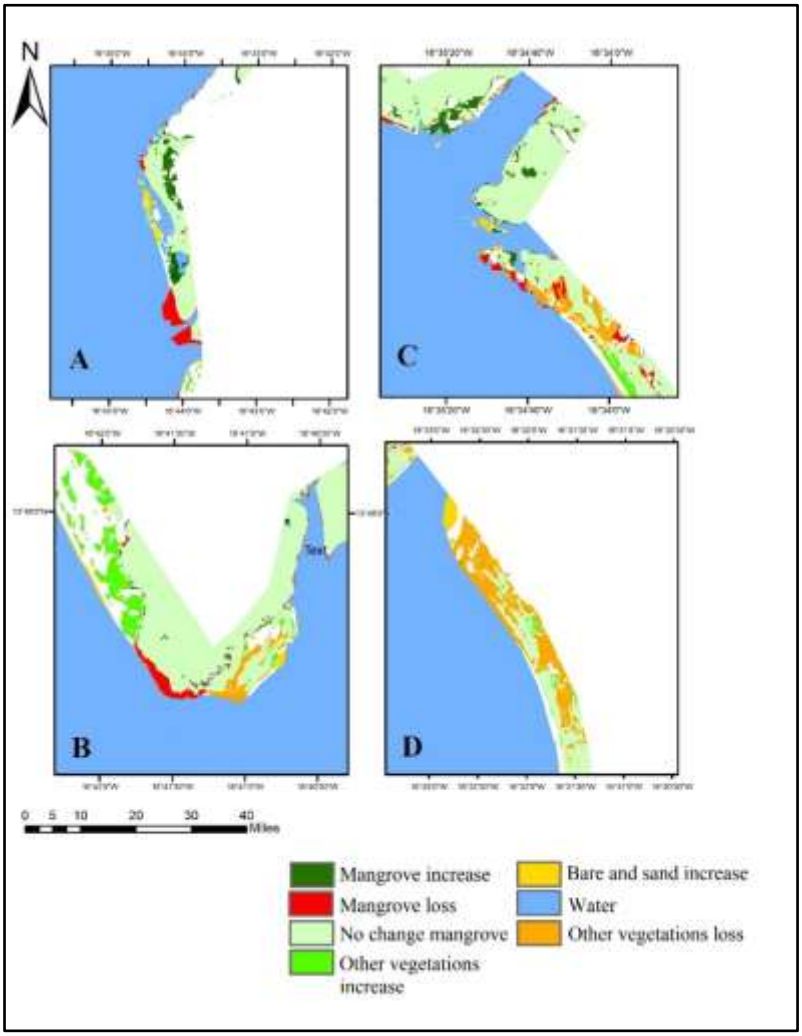

Figure 9: Areas of major change from 2000 to 2020

5. DISCUSSION

5.1. Shoreline dynamic

Our results show an annual average erosion rate of 2.44 m and an average accretion rate of 1.84 m. This rate of erosion is somewhat closer to the one reported by (Diadhiou et al. (2016) with an average rate of erosion of 2.60 m/yr in Palmarin between 1954–2018. By contrast, the rate of erosion is different from Sy, 2007, (as cited in Diadhiou et al., 2016) with 0.09 m/yr and from Diadhiou et al. (2016) with 0.82 m/yr. In the St-Louis region, Faye (2010) found an average rate of erosion of 1,70 m/yr. Exceptional erosion values up to 97–137 m/yr were reported for the langue de Barbarie and Sangomar Point, caused by specific coastal phenomena (Enríquez-de-Salamanca, 2020). The Saloum Delta coast is particularly sensitive to climatic hazards and natural phenomena such as erosion. A major extreme event permanently disrupted this ecosystem in 1987. The breach thus caused by this storm has widened over time and now exposes the villages of the islands to the ocean and, in particular, to the phenomenon of erosion (Bah et al., 2019).

The sectoral analysis has shown an average erosion of 2.82 m/yr in section E. This result is different from Bah et al.(2019)'s value which is 3.43 m/yr. Diadhiou et al.(2016) calculated an average rate of 3.83 m/yr along the Palmarin-Djiffer shore. This difference may be due to the time intervals chosen and the methodology used. No past study highlighted the rate of the shoreline change for sections D, C, B, and A. Nevertheless, our result, showing the dominance of erosion in this region, is conformed to the

International Journal of Current Science Research and Review
ISSN: 2581-8341
Volume 08 Issue 10 October 2025
DOI: 10.47191/ijcsrr/V8-i10-18, Impact Factor: 8.048
IJCSRR @ 2025
www.ijcsrr.org

trend of erosion observed in some sections. Studies conducted in sections C, D, and E estimated a total eroded surface of 3,111,131.88 m^2, together with an accretion surface of 2,286,958.36 m^2. The sediment balance was, therefore, negative, with a deficit of 824 173.52 m^2 in 33 years (Bah et al., 2019). In section A, our results have shown a tendency toward accretion. According to the PWM (2020), Jinack island and the mosaic of islands to the north are essentially shifting shoals of sand, resulting in accretion. Much of this accretion is the result of erosion further south. Anecdotal information stated that the beach in front of Madiyana Camp (Jinack shoreline) had been eroded more than 15m in the past years.

5.2. Vegetation dynamic

The mangroves of the Grand Saloum experienced spatial expansion between 2000 and 2020. Previous findings have confirmed this result (Andrieu et al., 2020; Fent et al., 2019; Lombard, 2021; Sakho et al., 2011). Finding in other wetlands ecosystem over the Gambia, like the TWNP, has shown a decrease from 1973 to 2012. This decrease is due to the long-term hyper-salinity that cause the lack of mangrove rejuvenation (Ceesay et al., 2017).

The other vegetation experienced loss from 2000 to 2020. Some vegetation cover such as lowland rice fields are exposed to salt intrusion (Dia, 2012). Salt intrusion into potential rice-growing zones is also very active in the Grand Saloum which is impacting the livelihoods of the local communities (WOW, 2015). The spatial distribution of forested wetland loss appears more consistent with saltwater intrusion (Bhattachan et al., 2018).

The results of the vegetation dynamics show that even if, globally, mangrove areas have continuously increased from 2000 to 2020, some parts close to the shoreline are experiencing loss. The Grand Saloum AWP (2020) reported that there are pockets of regression in places such as the coastal fringe exposed to erosion. The main driving forces contributing to the regression of mangrove cover are the rainfall deficit, water salinity, land acidification, coastal erosion, and unsustainable mangrove resource exploitation practices (ADG, 2012).

CONCLUSION

This transboundary assessment shows a coastline under persistent pressure but with encouraging signs of ecological resilience. Over 1990–2020, shoreline trajectories across the Grand Saloum are dominated by erosion (mean −2.44 $m \cdot yr^{-1}$) with localized accretion (mean +1.84 $m \cdot yr^{-1}$). Sectors C and D concentrate the highest retreat, while A and E exhibit mixed erosion–accretion hotspots and B remains comparatively less dynamic. Against this geomorphic backdrop, mangrove cover expanded from 57,867.61 ha to 66,840.17 ha between 2000 and 2020 (≈ +15.5%), even as “other vegetation” declined from 23,483.18 ha to 16,146.11 ha (≈ −31.3%). Within the 1 km coastal buffer, mangroves remained broadly stable with a slight net increase (16.43% to 16.81%), while other vegetation fluctuated with an overall downward tendency. Taken together, the findings suggest that mangrove gains, likely mediated by species- and site-specific tolerance, sediment supply, and restoration. In sum, the Grand Saloum remains dynamic yet resilient: mangroves are generally holding or advancing despite pervasive shoreline change. Acting now to secure inland migration pathways, manage high-erosion reaches, and operationalize a shared, science-based monitoring system will convert that resilience into long-term coastal protection, livelihoods, and carbon benefits for both Senegal and The Gambia.

REFERENCES

1. ADG. (2012). PRIORITY ACTION PLAN OF THE GRAND SALOUM OF THE FIRST YEAR OF THE PROJECT: Senegal Mangrove Forest Management Project from Senegal to Benin. 0–32.
2. Ajaj, Q. M., Pradhan, B., Noori, A. M., & Jebur, M. N. (2017). Spatial Monitoring of Desertification Extent in Western Iraq using Landsat Images and GIS. Land Degradation and Development, 28(8), 2418–2431. https://doi.org/10.1002/ldr.2775
3. Andrieu, J., Lombard, F., Fall, A., Thior, M., Ba, B. D., & Dieme, B. E. A. (2020). Botanical field-study and remote sensing to describe mangrove resilience in the Saloum Delta (Senegal) after 30 years of degradation narrative. Forest Ecology and Management, 461(December 2019), 117963. https://doi.org/10.1016/j.foreco.2020.117963
4. Bah, A., Ibrahima, C., & Noblet, M. (2019). Evaluation de la vulnérabilité du secteur agricole à la variabilité et aux changements climatiques dans la région de Fatick Secteur : Agriculture Projet d ’ Appui Scientifique aux processus de Plans Nationaux d ’ Adaptation . January, 123.
5. Bartuś, T. (2014). Raster images generalization in the context of research on the structure of landscape and geodiversity.

International Journal of Current Science Research and Review
ISSN: 2581-8341
Volume 08 Issue 10 October 2025
DOI: 10.47191/ijcsrr/V8-i10-18, Impact Factor: 8.048
IJCSRR @ 2025
www.ijcsrr.org

Geology, Geophysics & Environment, 40(3), 271. https://doi.org/10.7494/GEOL.2014.40.3.271

6. Bhattachan, A., Emanuel, R. E., Ardón, M., Bernhardt, E. S., Anderson, S. M., Stillwagon, M. G., Ury, E. A., Bendor, T. K., & Wright, J. P. (2018). Evaluating the effects of land-use change and future climate change on vulnerability of coastal landscapes to saltwater intrusion.
7. Ceesay, A., Hypolite Dibi, N., Njie, E., Wolff, M., & Koné, T. (2017). Mangrove Vegetation Dynamics of the Tanbi Wetland National Park in The Gambia. Environment and Ecology Research, 5(2), 145–160. https://doi.org/10.13189/eer.2017.050209
8. Chmiel, J., Kay, S., & Spruyt, P. (2004). Orthorectification and Geometric Quality Assessment of Very High Spatial Resolution Satellite Imagery for Common Agricultural Policy Purposes. Policy.
9. Church, J. A., Gregory, J. M., Huybrechts, P., Kuhn, M., Lambeck, K., Nhuan, M. T., Qin, D., & Woodworth, P. L. (2001). Changes in Sea Level Co-ordinating Lead Authors. 641–684.
10. Dia, M. I. (2012). Vulnerability Assessment of Central Coast Senegal (Saloum) and The Gambia Marine Coast and Estuary to Climate Change Induced Effects. Coastal Resources Center and WWF-WAMPO, April, 1–40.
11. Diadhiou, Y. B., Ndour, A., Niang, I., & Niang-Fall, A. (2016). Étude comparative de l'évolution du trait de côte sur deux flèches sableuses de la Petite Côte (Sénégal) : cas de Joal et de Djiffère. Norois, 240, 25–42. https://doi.org/10.4000/norois.5935
12. Diop, S., Barusseau, J.-P., & Descamps, C. (2014). The land/ocean interactions in the coastal zone of West and Central Africa. 210.
13. Drame, A., & Sambou, B. (2013). THE VULNERABILITY OF COMMUNITIES AROUND THE MARINE PROTECTED AREAS OF BAMBOUNG, CAYAR AND JOAL-FADIOUTH IN SENEGAL: PLACES OF ADAPTATION TO CLIMATE CHANGE. Senegal PARKS, 19(2). www.iucn.org/parks
14. Ellison, J. C. (2014). Vulnerability assessment of mangroves to climate change and sea-level rise impacts. Wetlands Ecology and Management 2014 23:2, 23(2), 115–137. https://doi.org/10.1007/S11273-014-9397-8
15. Enríquez-de-Salamanca, Á. (2020). Evolution of coastal erosion in Palmarin (Senegal). Journal of Coastal Conservation, 24(2), 25. https://doi.org/10.1007/s11852-020-00742-y
16. Faye, I. B. N. (2010). Dynamique du trait de côte sur les littoraux sableux de la Mauritanie à la Guinée-Bissau (Afrique de l'Ouest) : Approches régionale et locale par photo-interprétation, traitement d'images et analyse de cartes anciennes. Volume 1. 321.
17. Fent, A., Bardou, R., Carney, J., & Cavanaugh, K. (2019). Transborder political ecology of mangroves in Senegal and The Gambia. Global Environmental Change, 54(December 2018), 214–226. https://doi.org/10.1016/j.gloenvcha.2019.01.003
18. Friess, D. A., Krauss, K. W., Horstman, E., Balke, T., Bouma, T. J., Galli, D., & Webb, E. L. (2012). Are all intertidal wetlands naturally created equal? Bottlenecks, thresholds and knowledge gaps to mangrove and saltmarsh ecosystems. Biological Reviews, 87(2), 346–366. https://doi.org/10.1111/J.1469-185X.2011.00198.X
19. Hackman, K. O., Gong, P., & Wang, J. (2017). New land-cover maps of Ghana for 2015 using landsat 8 and three popular classifiers for biodiversity assessment. International Journal of Remote Sensing, 38(14), 4008–4021. https://doi.org/10.1080/01431161.2017.1312619
20. IPCC. (2007). Climate Change 2007. 10.
21. IPCC. (2023). Climate Change 2023 Synthesis Report. Atmosphere, 13(3), 35–115. https://doi.org/10.3390/atmos13030405
22. Jallow, B. P., Barrow, M. K. A., & Leatherman, S. P. (1996). Vulnerability of the coastal zone of the Gambia to sea level rise and development of response strategies and adaptation options. Climate Research, 6(2), 165–177. https://doi.org/10.3354/cr006165
23. Ji, L., Zhang, L., & Wylie, B. (2009). Analysis of Dynamic Thresholds for the Normalized Difference Water Index.
24. Jia, K., Wei, X., Gu, X., Yao, Y., Xie, X., & Li, B. (2014). Land cover classification using Landsat 8 Operational Land Imager data in Beijing, China. Https://Doi.Org/10.1080/10106049.2014.894586, 29(8), 941–951. https://doi.org/10.1080/10106049.2014.894586
25. Lombard, F. (2021). Mapping Mangrove Zonation Changes in Senegal with Landsat Imagery Using an OBIA Approach

International Journal of Current Science Research and Review
ISSN: 2581-8341
Volume 08 Issue 10 October 2025
DOI: 10.47191/ijcsrr/V8-i10-18, Impact Factor: 8.048
IJCSRR @ 2025
www.ijcsrr.org

Combined with Linear Spectral Unmixing.

26. McFEETERS, S. K. (1996). The use of the Normalized Difference Water Index (NDWI) in the delineation of open water features. Https://Doi.Org/10.1080/01431169608948714, 17(7), 1425–1432. https://doi.org/10.1080/01431169608948714
27. MEPN. (2006). Plan d'Action National pour l'adaptation aux changements climatiques. https://unfccc.int/resource/docs/napa/sen01f.pdf
28. Niang, I., Dansokho, M., Faye, S., Gueye, K., & Ndiaye, P. (2010). Impacts of climate change on the Senegalese coastal zones: Examples of the Cap Vert peninsula and Saloum estuary. Global and Planetary Change, 72(4), 294–301. https://doi.org/10.1016/J.GLOPLACHA.2010.01.005
29. P. W. Bakhoum, A. Ndour, I. Niang, B. Sambou, V. B. Traore, A. T. Diaw, H. Sambou, & M. L. Ndiaye. (2017). Coastline Mobility of Goree Island (Senegal), from 1942 to 2011. Marine Science, 7 No. 1, 1–9. http://article.sapub.org/10.5923.j.ms.20170701.01.html
30. PWM. (2020). NIUMI NATIONAL PARK MANAGEMENT PLAN 2020-2025. 49.
31. Sakho, I., Mesnage, V., Deloffre, J., La, R., Niang, I., & Faye, G. (2011). Estuarine , Coastal and Shelf Science The in fl uence of natural and anthropogenic factors on mangrove dynamics over 60 years : The Somone Estuary , Senegal. 94, 93–101. https://doi.org/10.1016/j.ecss.2011.05.032
32. Sekovski, I., Stecchi, F., Mancini, F., & Rio, L. Del. (2014). Image classification methods applied to shoreline extraction on very high-resolution multispectral imagery. Http://Dx.Doi.Org/10.1080/01431161.2014.907939, 35(10), 3556–3578. https://doi.org/10.1080/01431161.2014.907939
33. SIDIBE, A. (2010). Evaluation-Test sur l'utilisation de la Liste Rouge de l'UICN comme outil de suivi des risques de perte de biodiversité : Application aux espèces de poissons démersaux côtiers exploités en Afrique du Nord Ouest. 1–67.
34. Sow, E. H., & Ba, T. (2019). Evolution de la Mangrove de la Reserve de Biosphere du Delta du Saloum, Senegal. European Scientific Journal ESJ, 15(15). https://doi.org/10.19044/ESJ.2019.V15N15P467
35. Themistocleous, K., Hadjimitsis, D. G., Hadjimitsis, D. G., & Themistocleous, K. (2008). The importance of considering atmospheric correction in the pre-processing of satellite remote sensing data intended for the management and detection of cultural sites: a case stud International trade View project Climate change/ Adaptation View project T. October. https://www.researchgate.net/publication/257067491
36. Toure, S. I., Stow, D. A., Shih, H. chien, Weeks, J., & Lopez-Carr, D. (2018). Land cover and land use change analysis using multi-spatial resolution data and object-based image analysis. Remote Sensing of Environment, 210(March), 259–268. https://doi.org/10.1016/j.rse.2018.03.023
37. WOW. (2015). MANAGEMENT PLAN NIUMI-SALOUM TRANSBOUNDARY (THE GAMBIA - SENEGAL) (Issue September 2011).
38. Yu, L., Wang, J., & Gong, P. (2013). Improving 30 m global land-cover map FROM-GLC with time series MODIS and auxiliary data sets: A segmentation-based approach. International Journal of Remote Sensing, 34(16), 5851–5867. https://doi.org/10.1080/01431161.2013.798055

Cite this Article: Badji,O., Ceesay, A., Hackman, K.O. (2025). Geospatial Assessment of Three Decades of Shoreline Shifts and Two Decades of Vegetation Change in the Grand Saloum Transboundary Wetland Complex, Senegal-The Gambia. International Journal of Current Science Research and Review, 8(10), pp. 5048-5061. DOI: https://doi.org/10.47191/ijcsrr/V8-i10-18